B
APPENDIX

An Illustration and Exercise of Computational Fluid Dynamics

The purpose of this appendix is to give the interested reader an opportunity for a hands-on experience in computational fluid dynamics (CFD). In various chapters of this book, computational fluid dynamics is discussed in the context of *modern* compressible flow. It is not our purpose, however, to present CFD in any detail; rather, this book emphasizes the *physical* aspects of compressible flow. Indeed, computation fluid dynamics is a subject by itself, and the reader is encouraged to examine the number of texts devoted exclusively to CFD.

On the other hand, this appendix offers the opportunity to sample the essence of CFD through an example using MacCormack's time-marching explicit finite-difference technique—by far the most "student-friendly" CFD technique that can be found. The application is the subsonic-supersonic quasi-one-dimensional isentropic flow through a convergent-divergent nozzle—the CFD application discussed in Sec. 12.1. In this appendix we go into the details that produced the results given in Sec. 12.1. This example is the simplest possible exercise that reflects the essence of CFD, yet you will find its explanation requires a rather lengthy discussion. Any other example of CFD goes well beyond the scope of this book.

Finally, for a very basic introduction to CFD, you are encouraged to examine the author's book *Computational Fluid Dynamics: The Basics with Applications,* McGraw-Hill, 1995, which contains a number of worked examples in elementary CFD, including the one described in this appendix. What follows is excerpted from Chap. 7 of that book. This is the author's best attempt to provide you with a hands-on experience in CFD. The appendix ends with a FORTRAN code listing that the author wrote for this particular application.

THE EQUATIONS

Return to Sec. 12.1 and review the basic governing equations for unsteady quasi-one-dimensional flow, namely, Eqs. (12.5), (12.6), and (12.7)—the continuity, momentum,

and energy equations, respectively. Assuming a calorically perfect gas, let us replace the internal energy in Eq. (12.7) with temperature. For a calorically perfect gas

$$e = c_v T$$

Hence, Eq. (12.7) becomes

$$\rho c_v \frac{\partial T}{\partial t} + \rho u c_v \frac{\partial T}{\partial x} = -p \frac{\partial u}{\partial x} - pu \frac{\partial (\ln A)}{\partial x}$$ (B.1)

As an interim summary, our continuity, momentum, and energy equations for unsteady, quasi-one-dimensional flow are given by Eqs. (12.5), (12.6), and (B.1), respectively. Take the time to look at these equations; you see three equations with four unknown variables ρ, u, p, and T. The pressure can be eliminated from these equations by using the equation of state

$$p = \rho R T$$ (B.2)

along with its derivative

$$\frac{\partial p}{\partial x} = R \left(\rho \frac{\partial T}{\partial x} + T \frac{\partial \rho}{\partial x} \right)$$ (B.3)

With this, we expand Eq. (12.5) and rewrite Eqs. (12.6) and (B.1), respectively, as

Continuity: $$\frac{\partial (\rho A)}{\partial t} + \rho A \frac{\partial u}{\partial x} + \rho u \frac{\partial A}{\partial x} + u A \frac{\partial \rho}{\partial x} = 0$$ (B.4)

Momentum: $$\rho \frac{\partial u}{\partial t} + \rho u \frac{\partial u}{\partial x} = -R \left(\rho \frac{\partial T}{\partial x} + T \frac{\partial \rho}{\partial x} \right)$$ (B.5)

Energy: $$\rho c_v \frac{\partial T}{\partial t} + \rho u c_v \frac{\partial T}{\partial x} = -\rho R T \left[\frac{\partial u}{\partial x} + u \frac{\partial (\ln A)}{\partial x} \right]$$ (B.6)

At this stage, we could readily proceed to set up our numerical solution of Eqs. (B.4) to (B.6). Note that these are written in terms of dimensional variables. This is fine, and many CFD solutions are carried out directly in terms of such dimensional variables. Indeed, this has an added engineering advantage because it gives you a feeling for the magnitudes of the real physical quantities as the solution progresses. However, for nozzle flows, the flowfield variables are frequently expressed in terms of nondimensional variables, where the flow variables are referenced to their reservoir values. The nondimensional variables p/p_o, ρ/ρ_o, and T/T_o vary between 0 and 1, which is an "aesthetic" advantage when presenting the results. Because fluid dynamicists dealing with nozzle flows so frequently use these nondimensional terms, we will follow suit here. (A number of CFD practitioners prefer to always deal with nondimensional variables, whereas others prefer dimensional variables; as far as the numerics are concerned, there should be no real difference, and the choice is really a matter of your personal preference.) Therefore, we define the

nondimensional temperature and density, respectively, as

$$T' = \frac{T}{T_o} \qquad \rho' = \frac{\rho}{\rho_o}$$

where (for the time being) the prime denotes a dimensionless variable. Moreover, letting L denote the length of the nozzle, we define a dimensionless length as

$$x' = \frac{x}{L}$$

Denoting the speed of sound in the reservoir as a_o, where

$$a_o = \sqrt{\gamma R T_o}$$

we define a dimensionless velocity as

$$V' = \frac{u}{a_o}$$

Also, the quantity L/a_o has the dimension of time, and we define a dimensionless time as

$$t' = \frac{t}{L/a_o}$$

Finally, we ratio the local area A to the sonic throat area A^* and define a dimensionless area as

$$A' = \frac{A}{A^*}$$

Returning to Eq. (B.4) and introducing the nondimensional variables, we have

$$\frac{\partial(\rho' A')}{\partial t'} \left(\frac{\rho_o A^*}{L/a_o} \right) + \rho' A' \frac{\partial V'}{\partial x'} \left(\frac{\rho_o A^* a_o}{L} \right) + \rho' V' \frac{\partial A'}{\partial x'} \left(\frac{\rho_o a_o A^*}{L} \right)$$

$$+ V' A' \frac{\partial \rho'}{\partial x'} \left(\frac{a_o A^* \rho_o}{L} \right) = 0 \qquad \text{(B.7)}$$

Note that A' is a function of x' only; it is *not* a function of time (the nozzle geometry is fixed, invariant with time). Hence, in Eq. (B.7) the time derivative can be written as

$$\frac{\partial(\rho' A')}{\partial t'} = A' \frac{\partial \rho'}{\partial t'}$$

With this, Eq. (B.7) becomes

Continuity:
$$\boxed{\frac{\partial \rho'}{\partial t'} = -\rho' \frac{\partial V'}{\partial x'} - \rho' V' \frac{\partial(\ln A')}{\partial x'} - V' \frac{\partial \rho'}{\partial x'}} \qquad \text{(B.8)}$$

Returning to Eq. (B.5) and introducing the nondimensional variables, we have

$$\rho'\frac{\partial V'}{\partial t'}\left(\frac{\rho_o a_o}{L/a_o}\right) + \rho'V'\frac{\partial V'}{\partial x'}\left(\frac{\rho_o a_o^2}{L}\right) = -R\left(\rho'\frac{\partial T'}{\partial x'} + T'\frac{\partial \rho'}{\partial x'}\right)\left(\frac{\rho_o T_o}{L}\right)$$

or

$$\rho'\frac{\partial V'}{\partial t'} = -\rho'V'\frac{\partial V'}{\partial x'} - \left(\rho'\frac{\partial T'}{\partial x'} + T'\frac{\partial \rho'}{\partial x'}\right)\frac{RT_o}{a_o^2} \tag{B.9}$$

In Eq. (B.9), note that

$$\frac{RT_o}{a_o^2} = \frac{\gamma RT_o}{\gamma a_o^2} = \frac{a_o^2}{\gamma a_o^2} = \frac{1}{\gamma}$$

Hence, Eq. (B.9) becomes

Momentum:
$$\boxed{\frac{\partial V'}{\partial t'} = -V'\frac{\partial V'}{\partial x'} - \frac{1}{\gamma}\left(\frac{\partial T'}{\partial x'} + \frac{T'}{\rho'}\frac{\partial \rho'}{\partial x'}\right)} \tag{B.10}$$

Returning to Eq. (B.6) and introducing the nondimensional variables, we have

$$\rho'c_v\frac{\partial T'}{\partial t'}\left(\frac{\rho_o T_o}{L/a_o}\right) + \rho'V'c_v\frac{\partial T'}{\partial x'}\left(\frac{\rho_o a_o T_o}{L}\right)$$

$$= -\rho'RT'\left[\frac{\partial V'}{\partial x'} + V'\frac{\partial(\ln A')}{\partial x'}\right]\left(\frac{\rho_o T_o a_o}{L}\right) \tag{B.11}$$

In Eq. (B.11), the factor R/c_v is given by

$$\frac{R}{c_v} = \frac{R}{R/(\gamma - 1)} = \gamma - 1$$

Hence, Eq. (B.11) becomes

Energy:
$$\boxed{\frac{\partial T'}{\partial t'} = -V'\frac{\partial T'}{\partial x'} - (\gamma - 1)T'\left[\frac{\partial V'}{\partial x'} + V'\frac{\partial(\ln A')}{\partial x'}\right]} \tag{B.12}$$

That is it! After what may seem like an interminable manipulation of the governing equations, we have finally set up that particular form of the equations that will be most appropriate as well as convenient for the time-marching solution of quasi-one-dimensional nozzle flow, namely, Eqs. (B.8), (B.10), and (B.12).

The Finite-Difference Equations

We now proceed to the setting up of the finite-difference expressions using MacCormack's explicit technique for the numerical solution of Eqs. (B.8), (B.10), and (B.12). To implement a finite-difference solution, we divide the x axis along the nozzle into a number of discrete grid points, as shown in Fig. B.1. (Recall that in our quasi-one-dimensional nozzle assumption, the flow variables *across* the nozzle cross section at any particular grid point, say point i, are uniform.) In Fig. B.1, the first grid point, labeled point 1, is assumed to be in the reservoir. The points are evenly distributed along the x axis, with Δx denoting the spacing between grid points. The
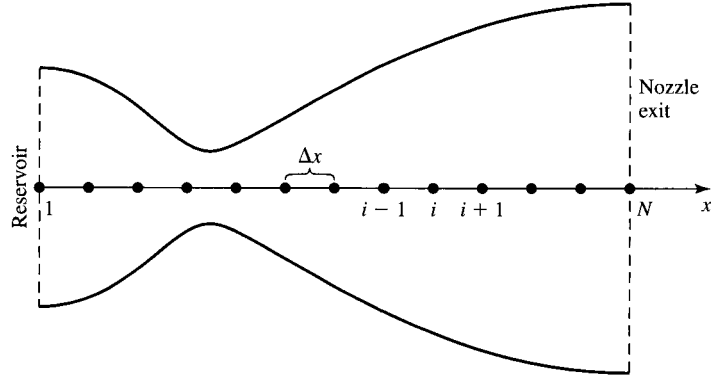
Figure B.1 | Grid point distribution along the nozzle.

last point, namely, that at the nozzle exit, is denoted by N; we have a total number of N grid points distributed along the axis. Point i is simply an arbitrary grid point, with points $i-1$ and $i+1$ as the adjacent points. Recall from Sec. 12.1 that MacCormack's technique is a predictor-corrector method. In the time-marching approach, remember that we know the flowfield variables at time t, and we use the difference equations to solve explicitly for the variables at time $t + \Delta t$.

First, consider the predictor step. Following the discussion in Sec. 12.1, we set up the spatial derivatives as forward differences. Also, to reduce the complexity of the notation, we will drop the use of the prime to denote a dimensionless variable. In what follows, *all* variables are the nondimensional variables, denoted earlier by the prime notation. From Eq. (B.8) we have

$$\left(\frac{\partial \rho}{\partial t}\right)_i^t = -\rho_i^t \frac{V_{i+1}^t - V_i^t}{\Delta x} - \rho_i^t V_i^t \frac{\ln A_{i+1} - \ln A_i}{\Delta x} - V_i^t \frac{\rho_{i+1}^t - \rho_i^t}{\Delta x} \quad \text{(B.13)}$$

From Eq. (B.10), we have

$$\left(\frac{\partial V}{\partial t}\right)_i^t = -V_i^t \frac{V_{i+1}^t - V_i^t}{\Delta x} - \frac{1}{\gamma}\left(\frac{T_{i+1}^t - T_i^t}{\Delta x} + \frac{T_i^t}{\rho_i^t}\frac{\rho_{i+1}^t - \rho_i^t}{\Delta x}\right) \quad \text{(B.14)}$$

From Eq. (B.12), we have

$$\left(\frac{\partial T}{\partial t}\right)_i^t = -V_i^t \frac{T_{i+1}^t - T_i^t}{\Delta x} - (\gamma - 1)T_i^t\left(\frac{V_{i+1}^t - V_i^t}{\Delta x} + V_i^t \frac{\ln A_{i+1} - \ln A_i}{\Delta x}\right)$$

$$\text{(B.15)}$$

We obtain predicted values of ρ, V, and T, denoted by barred quantities, from

$$\bar{\rho}_i^{t+\Delta t} = \rho_i^t + \left(\frac{\partial \rho}{\partial t}\right)_i^t \Delta t \quad \text{(B.16)}$$

$$\bar{V}_i^{t+\Delta t} = V_i^t + \left(\frac{\partial V}{\partial t}\right)_i^t \Delta t \quad \text{(B.17)}$$

$$\bar{T}_i^{t+\Delta t} = T_i^t + \left(\frac{\partial T}{\partial t}\right)_i^t \Delta t \quad \text{(B.18)}$$

In Eqs. (B.16) to (B.18), p_i^t, V_i^t, and T_i^t are known values at time t. Numbers for the time derivatives in Eqs. (B.16) to (B.18) are supplied directly by Eqs. (B.13) to (B.15)

Moving to the corrector step, we return to Eqs. (B.8), (B.10), and (B.12) and replace the spatial derivatives with rearward differences, using the predicted (barred) quantities. We have from Eq. (B.8)

$$
\left(\frac{\overline{\partial \rho}}{\partial t}\right)_i^{t+\Delta t} = -\bar{\rho}_i^{t+\Delta t}\frac{\bar{V}_i^{t+\Delta t} - \bar{V}_{i-1}^{t+\Delta t}}{\Delta x} - \bar{\rho}_i^{t+\Delta t}\bar{V}_i^{t+\Delta t}\frac{\ln A_i - \ln A_{i-1}}{\Delta x}
$$
$$
- \bar{V}_i^{t+\Delta t}\frac{\bar{\rho}_i^{t+\Delta t} - \bar{\rho}_{i-1}^{t+\Delta t}}{\Delta x}
$$
(B.19)

From Eq. (B.10), we have

$$
\left(\frac{\overline{\partial V}}{\partial t}\right)_i^{t+\Delta t} = -\bar{V}_i^{t+\Delta t}\frac{\bar{V}_i^{t+\Delta t} - \bar{V}_{i-1}^{t+\Delta t}}{\Delta x}
$$
$$
- \frac{1}{\gamma}\left(\frac{\bar{T}_i^{t+\Delta t} - \bar{T}_{i-1}^{t+\Delta t}}{\Delta x} + \frac{\bar{T}_i^{t+\Delta t}}{\bar{\rho}_i^{t+\Delta t}}\frac{\bar{\rho}_i^{t+\Delta t} - \bar{\rho}_{i-1}^{t+\Delta t}}{\Delta x}\right)
$$
(B.20)

From Eq. (B.12), we have

$$
\left(\frac{\overline{\partial T}}{\partial t}\right)_i^{t+\Delta t} = -\bar{V}_i^{t+\Delta t}\frac{\bar{T}_i^{t+\Delta t} - \bar{T}_{i-1}^{t+\Delta t}}{\Delta x} - (\gamma - 1)\bar{T}_i^{t+\Delta t}
$$
$$
\times\left(\frac{\bar{V}_i^{t+\Delta t} - \bar{V}_{i-1}^{t+\Delta t}}{\Delta x} + \bar{V}_i^{t+\Delta t}\frac{\ln A_i - \ln A_{i-1}}{\Delta x}\right)
$$
(B.21)

The average time derivatives are given by

$$
\left(\frac{\partial \rho}{\partial t}\right)_{av} = 0.5\left[\underbrace{\left(\frac{\partial \rho}{\partial t}\right)_i^t}_{\substack{\text{From}\\ \text{Eq. (B.13)}}} + \underbrace{\left(\frac{\overline{\partial \rho}}{\partial t}\right)_i^{t+\Delta t}}_{\substack{\text{From}\\ \text{Eq. (B.19)}}}\right]
$$
(B.22)

$$
\left(\frac{\partial V}{\partial t}\right)_{av} = 0.5\left[\underbrace{\left(\frac{\partial V}{\partial t}\right)_i^t}_{\substack{\text{From}\\ \text{Eq. (B.14)}}} + \underbrace{\left(\frac{\overline{\partial V}}{\partial t}\right)_i^{t+\Delta t}}_{\substack{\text{From}\\ \text{Eq. (B.20)}}}\right]
$$
(B.23)

$$
\left(\frac{\partial T}{\partial t}\right)_{av} = 0.5\left[\underbrace{\left(\frac{\partial T}{\partial t}\right)_i^t}_{\substack{\text{From}\\ \text{Eq. (B.15)}}} + \underbrace{\left(\frac{\overline{\partial T}}{\partial t}\right)_i^{t+\Delta t}}_{\substack{\text{From}\\ \text{Eq. (B.21)}}}\right]
$$
(B.24)

Finally, we have for the corrected values of the flowfield variables at time $t + \Delta t$

$$\rho_i^{t+\Delta t} = \rho_i^t + \left(\frac{\partial \rho}{\partial t}\right)_{av} \Delta t \tag{B.25}$$

$$V_i^{t+\Delta t} = V_i^t + \left(\frac{\partial V}{\partial t}\right)_{av} \Delta t \tag{B.26}$$

$$T_i^{t+\Delta t} = T_i^t + \left(\frac{\partial T}{\partial t}\right)_{av} \Delta t \tag{B.27}$$

Keep in mind that all the variables in Eqs. (B.13) to (B.27) are the *nondimensional* values. Also, Eqs. (B.13) to (B.27) constitute the finite-difference expressions of the governing equations in a form that pertains to MacCormack's technique.

Calculation of Time Step

We now proceed to the setting up of other details necessary for the numerical solution of the quasi-one-dimensional nozzle flow problem. First, we ask the question: What about the magnitude of Δt? The governing system of equations, Eqs. (B.4) to (B.6), is hyperbolic with respect to time. A stability constraint exists on this system, namely,

$$\Delta t = C \frac{\Delta x}{a + V} \tag{B.28}$$

where C is the *Courant number;* the simple stability analysis of a linear hyperbolic equation gives the result that $C \leq 1$ for an explicit numerical solution to be stable. The present application to subsonic-supersonic isentropic nozzle flow is governed by *nonlinear* partial differential equations, namely, Eqs. (B.8), (B.10), and (B.12). In this case, the exact stability criterion for a linear equation, namely, that $C \leq 1$, can only be viewed as general guidance for our present nonlinear problem. However, it turns out to be quite good guidance, as we shall see. Equation (B.28) is the *Courant-Friedrichs-Lowry (CFL) criterion* for a one-dimensional flow, where V is the local flow velocity at a point in the flow and a is the local speed of sound. Equation (B.28), along with $C \leq 1$, simply states that Δt must be less than, or at best equal to, the time it takes a sound wave to move from one grid point to the next. Note that t, x, a, and V are nondimensionalized. The nondimensional form of Eq. (B.28) is exactly the same form as the dimensional case. (Prove this to yourself.) Hence, we will hereafter treat the variables in Eq. (B.28) as our nondimensional variables defined earlier. That is, in Eq. (B.28), Δt is the increment in nondimensional time and Δx is the increment in nondimensional space; Δt and Δx in Eq. (B.28) are precisely the same as appear in the nondimensional equations (B.13) to (B.27). Examining Eq. (B.28) more carefully, we note that, although Δx is the same throughout the flow, both V and a are variables. Hence, at a given grid point at a given time step, Eq. (B.28) is written as

$$(\Delta t)_i^t = C \frac{\Delta x}{a_i^t + V_i^t} \tag{B.29}$$

At an adjacent grid point, we have from Eq. (B.28)

$$(\Delta t)^t_{i+1} = C \frac{\Delta x}{a^t_{i+1} + V^t_{i+1}} \tag{B.30}$$

Clearly, $(\Delta t)^t_i$ and $(\Delta t)^t_{i+1}$ obtained from Eqs. (B.29) and (B.30), respectively are, in general, different values. Hence, in the implementation of the time-marching solution, we have two choices:

1. In utilizing Eqs. (B.16) to (B.18) and (B.25) to (B.27), we can, at each grid point i, employ the *local* values of $(\Delta t)^t_i$ determined from Eq. (B.29). In this fashion, the flowfield variables at each grid point in Fig. B.1 will be advanced in time according to their own, local time step. Hence, the resulting flowfield at time $t + \Delta t$ will be in a type of *artificial "time warp,"* with the flowfield variables at a given grid point corresponding to some nonphysical time different from that of the variables at an adjacent grid point. Clearly, such a *local time-stepping* approach does not realistically follow the *actual, physical transients* in the flow and hence cannot be used for an accurate solution of the *unsteady* flow. However, if the final steady-state flowfield in the limit of large time is the only desired result, then the intermediate variation of the flowfield variables with time is irrelevant. Indeed, if such is the case, the *local* time-stepping will frequently lead to *faster* convergence to the steady state. This is why some practitioners use the local time-stepping approach. However, there is always a philosophical question that arises here, namely, does the *local* time-stepping method always lead to the *correct* steady state? Although the answer is usually yes, there is still some reason for a small feeling of discomfort in this regard.

2. The other choice is to calculate $(\Delta t)^t_i$ at all the grid points, $i = 1$ to $i = N$, and then choose the *minimum* value for use in Eqs. (B.16) to (B.18) and (B.12) to (B.27). That is,

$$\Delta t = \text{minimum}\left(\Delta t^t_1, \Delta t^t_2, \ldots, \Delta t^t_i, \ldots, \Delta t^t_N\right) \tag{B.31}$$

The resulting Δt obtained from Eq. (B.31) is then used in Eqs. (B.16) to (B.18) and (B.25) to (B.27). In this fashion, the flowfield variables at all the grid points at time $t + \Delta t$ all correspond to the *same* physical time. Hence, the time-marching solution is following the actual unsteady flow variations that would exist in nature; i.e., the solution gives a time-accurate solution of the actual transient flowfield, consistent with the unsteady continuity, momentum, and energy equations. This consistent time-marching is the approach we will use in the present example. Although it may require more time steps to approach the steady state in comparison to the "local" time stepping described earlier, we can feel comfortable that the consistent time-marching approach is giving us the physically meaningful transient variations—which frequently are of intrinsic value by themselves. Thus, in our subsequent calculations, we will use Eq. (B.31) to determine the value of Δt.

Boundary Conditions

Another aspect of the numerical solution is that of *boundary conditions*—an all-important aspect, because without the physically proper implementation of boundary conditions and their numerically proper representation, we have no hope whatsoever in obtaining a proper numerical solution to our flow problem. Returning to Fig. B.1, we note that grid points 1 and N represent the two boundary points on the x axis. Point 1 is essentially in the reservoir; it represents an *inflow* boundary, with flow coming from the reservoir and entering the nozzle. In contrast, point N is an *outflow* boundary, with flow leaving the nozzle at the nozzle exit. Moreover, the flow velocity at point 1 is a very low, subsonic value. (The flow velocity at point 1, which corresponds to a finite area ratio A_1/A^*, cannot be precisely zero; if it were, there would be no mass flow entering the nozzle. Hence, point 1 does not correspond *exactly* to the reservoir, where by definition the flow velocity is zero. That is, the area for the reservoir is theoretically infinite, and we are clearly starting our own calculation at point 1 where the cross-sectional area is finite.) Hence, not only is point 1 an *inflow* boundary, it is a *subsonic* inflow boundary. *Question:* Which flow quantities should be specified at this subsonic inflow boundary and which should be calculated as part of the solution (i.e., allowed to "float" as a function of time)? A formal answer can be obtained by using the method of characteristics for an unsteady, one-dimensional flow, as introduced in Chap. 7. We did not develop the method of characteristics in Chap. 7 to the extent necessary to precisely study this question about the boundary conditions; indeed, such a matter is beyond the scope of this book. However, we will mention the result of such a study, which you will find to be physically acceptable. Unsteady, inviscid flow is governed by hyperbolic equations, and therefore for one-dimensional unsteady flow there exist two real characteristic lines through any point in the xt plane. Physically, these two characteristics represent infinitely weak Mach waves that are propagating upstream and downstream, respectively. Both Mach waves are traveling at the speed of sound a. Now turn to Fig. B.2, which shows our convergent-divergent nozzle (Fig. B.2a) with an xt diagram sketched below it (Fig. B.2b). Concentrate on grid point 1 in the xt plane in Fig. B.2b. At point 1, the local flow velocity is subsonic, $V_1 < a_1$. Hence, the left-running characteristic at point 1 travels *upstream,* to the left in Fig. B.2; i.e., the left-running Mach wave, which is traveling toward the left (relative to a moving fluid element) at the speed of sound easily works its way *upstream* against the low-velocity subsonic flow, which is slowly moving from left to right. Hence, in Fig. B.2b, we show the left-running characteristic running to the left with a combined speed $a_1 - V_1$ (relative to the fixed nozzle in Fig. B.2a). Since the domain for the flowfield to be calculated is contained between grid points 1 and N, then at point 1 we see that the left-running characteristic is propagating *out of* the domain; it is propagating to the left, away from the domain. In contrast, the right-running characteristic, which is a Mach wave propagating to the right at the speed of sound relative to a fluid element, is clearly moving toward the right in Fig. B.2b. This is for two reasons: (1) the fluid element at point 1 is already moving toward the right, and (2) the right-running Mach wave (characteristic) is moving toward the right at the speed of sound relative to the fluid element. Hence, the right-running characteristic is propagating to the right (relative to the
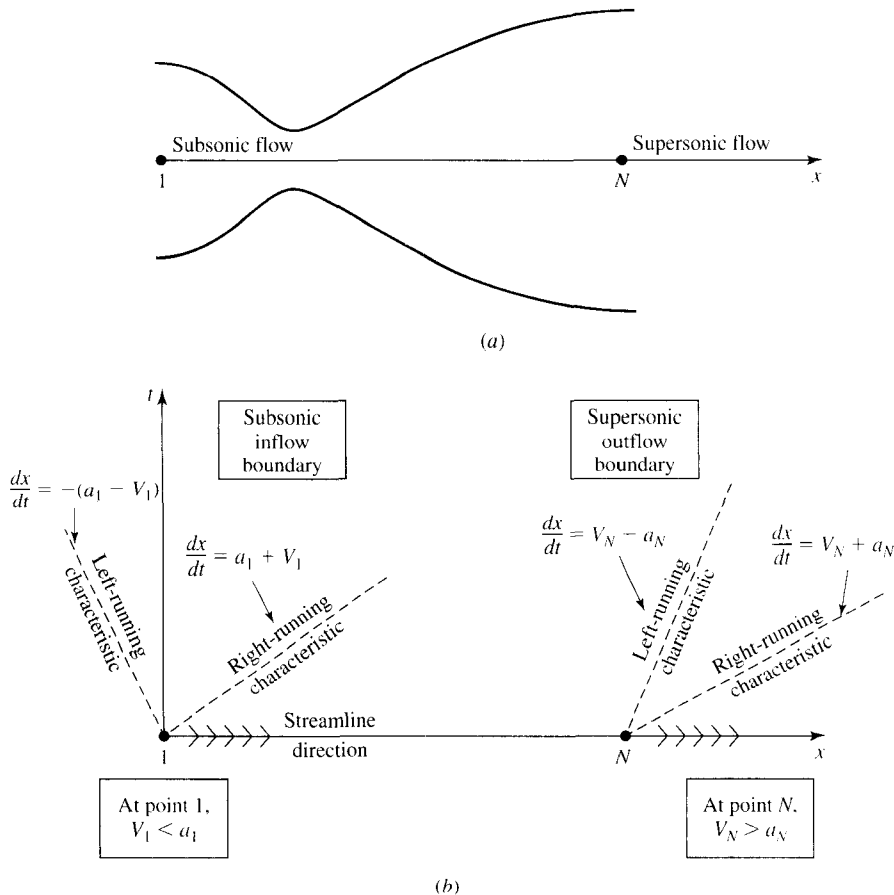
Figure B.2 | Study of boundary conditions: subsonic inflow and supersonic outflow.

nozzle) at a combined velocity of $V_1 + a_1$. What we see here is that the right-running characteristic is propagating from point 1 *into* the domain of the calculation.

What does all this have to do with boundary conditions? The method of characteristics tells us that at a boundary where one characteristic propagates *into* the domain, then the value of one dependent flowfield variable must be *specified* at that boundary, and if one characteristic line propagates *out* of the domain, then the value of another dependent flowfield variable must be allowed to *float* at the boundary; i.e., it must be calculated in steps of time as a function of the timewise solution of the flowfield. Also, note that at point 1 a streamline flows *into* the domain, across the inflow boundary. In terms of denoting what should and should not be specified at the boundary, the streamline *direction* plays the same role as the characteristic directions; i.e., the streamline moving *into* the domain at point 1 stipulates that the value of a second flowfield variable must be *specified* at the inflow boundary. *Conclusion:* At the *subsonic inflow boundary,* we must *stipulate* the values of *two* dependent

flowfield variables, whereas the value of *one* other variable must be allowed to *float*. (Please note that this discussion has been intentionally hand-waving and somewhat intuitive; a rigorous mathematical development is deferred for your future studies, beyond the scope of this book.)

Let us apply these ideas to the *outflow* boundary, located at grid point N in Fig. B.2. As before, the left-running characteristic at point N propagates to the left at the speed of sound a *relative to a fluid element*. However, because the speed of the fluid element itself is supersonic, the left-running characteristic is carried *downstream* at the speed (relative to the nozzle) of $V_N - a_N$. The right-running characteristic at point N propagates to the right at the speed of sound a relative to the fluid element, and thus it is swept downstream at the speed (relative to the nozzle) of $V_N + a_N$. Hence, at the *supersonic outflow boundary*, we have both characteristics propagating *out* of the domain; so does the streamline at point N. Therefore, there are *no* flowfield variables that require their values to be stipulated at the supersonic outflow boundary; *all* variables must be allowed to *float* at this boundary.

This discussion details how the inflow and outflow boundary conditions are to be handled on an *analytical* basis. The *numerical* implementation of this discussion is carried out as follows.

Subsonic Inflow Boundary (Point 1).   Here, we must allow one variable to float; we choose the velocity V_1, because on a physical basis we know the mass flow through the nozzle must be allowed to adjust to the proper steady state, and allowing V_1 to float makes the most sense as part of this adjustment. The value of V_1 changes with time and is calculated from information provided by the flowfield solution over the internal points. (The *internal* points are those *not* on a boundary, i.e., points 2 through $N - 1$ in Fig. B.1). We use linear extrapolation from points 2 and 3 to calculate V_1. This is illustrated in Fig. B.3. Here, the slope of the linear extrapolation line is determined from points 2 and 3 as

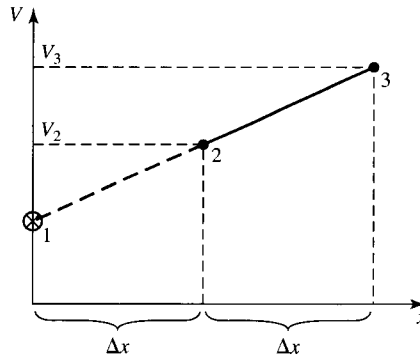$$\text{Slope} = \frac{V_3 - V_2}{\Delta x}$$

Figure B.3 | Sketch for linear extrapolation.

Using this slope to find V_1 by linear extrapolation, we have

$$V_1 = V_2 - \frac{V_3 - V_2}{\Delta x} \Delta x$$

or
$$V_1 = 2V_2 - V_3 \tag{B.32}$$

All other flowfield variables are specified. Since point 1 is viewed as essentially the reservoir, we stipulate the density and temperature at point 1 to be their respective stagnation values, ρ_o and T_o, respectively. These are held *fixed*, independent of time. Hence, in terms of the *nondimensional* variables, we have

$$\left.\begin{array}{l} \rho_1 = 1 \\[2mm] T_1 = 1 \end{array}\right\} \text{fixed, independent of time} \tag{B.33}$$

Supersonic Outflow Boundary (Point N).   Here, we must allow *all* flowfield variables to float. We again choose to use linear extrapolation based on the flowfield values at the internal points. Specifically, we have, for the *nondimensional* variables,

$$V_N = 2V_{N-1} - V_{N-2} \tag{B.34a}$$

$$\rho_N = 2\rho_{N-1} - \rho_{N-2} \tag{B.34b}$$

$$T_N = 2T_{N-1} - T_{N-2} \tag{B.34c}$$

Nozzle Shape and Initial Conditions

The nozzle shape, $A = A(x)$, is specified and held fixed, independent of time. For the case illustrated in this appendix, we choose a parabolic area distribution given by

$$A = 1 + 2.2(x - 1.5)^2 \qquad 0 \le x \le 3 \tag{B.35}$$

Note that $x = 1.5$ is the throat of the nozzle, that the convergent section occurs for $x < 1.5$, and that the divergent section occurs for $x > 1.5$. This nozzle shape is drawn to scale in Fig. B.4.

To start the time-marching calculations, we must stipulate *initial* conditions for ρ, T, and V as a function of x; that is, we must set up values of ρ, T, and V at time $t = 0$. In *theory*, these initial conditions can be purely arbitrary. In practice, there are two reasons why you want to choose the initial conditions *intelligently:*

1.   The closer the initial conditions are to the final steady-state answer, the faster the time-marching procedure will converge, and hence the shorter will be the computer execution time.

2.   If the initial conditions are too far away from reality, the initial timewise gradients at early time steps can become huge; i.e., the *time derivatives* themselves are initially very large. For a given time step Δt and a given spatial resolution Δx, it has been the author's experience that *inordinately* large gradients during the early part of the time-stepping procedure can cause the program to go unstable. In a sense, you can visualize the behavior of a
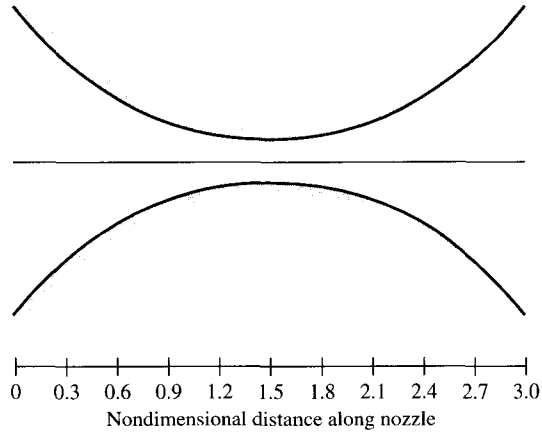
| | | | | | | | | | | |
|0|0.3|0.6|0.9|1.2|1.5|1.8|2.1|2.4|2.7|3.0|

Nondimensional distance along nozzle

Figure B.4 | Shape of the nozzle used for the present calculations. This geometric picture is not unique; for a calorically perfect gas, what is germane is the area ratio distribution along the nozzle. Hence, assuming a two-dimensional nozzle, the ordinates of the shape shown here can be ratioed by any constant factor, and the nozzle solution would be the same.

time-marching solution as a stretched rubber band. At early times, the rubber band is highly stretched, thus providing a *strong* potential to push the flowfield *rapidly* toward the steady-state solution. As time progresses, the flowfield gets closer to the steady-state solution, and the rubber band progressively relaxes, hence slowing down the rate of approach [i.e., at larger times, the values of the time derivatives calculated from Eqs. (B.22) to (B.24) become progressively smaller]. At the beginning of the calculation, it is wise not to pick initial conditions which are so far off that the rubber band is "stretched too far," and may even break.

Therefore, in your choice of initial conditions, you are encouraged to use *any* knowledge you may have about a given problem in order to intelligently pick some initial conditions. For example, in the present problem, we know that ρ and T *decrease* and V *increases* as the flow expands through the nozzle. Hence, we choose initial conditions that *qualitatively* behave in the same fashion. For simplicity, let us assume linear variations of the flowfield variables, as a function of x. For the present case, we assume these values at time $t = 0$.

$$\rho = 1 - 0.3146x \qquad\qquad\qquad\qquad\qquad\qquad\qquad\qquad (B.36a)$$

$$T = 1 - 0.2314x \quad \Big\} \text{ initial conditions at } t = 0 \qquad (B.36b)$$

$$V = (0.1 + 1.09x)T^{1/2} \qquad\qquad\qquad\qquad\qquad\qquad (B.36c)$$

INTERMEDIATE NUMERICAL RESULTS: THE FIRST FEW STEPS

In this section, we give a few numerical results that reflect the first stages of the calculation. This is to give you a more solid impression of what is going on and to provide some intermediate results for you to compare with when you write and run your own computer solution to this problem.

The first step is to feed the nozzle shape and the initial conditions into the program. These are given by Eqs. (B.35) and (B.36); the resulting numbers are tabulated in Table B.1. The values of ρ, V, and T given in this table are for $t = 0$.

The next step is to put these initial conditions into Eqs. (B.13) to (B.15) to initiate calculations pertaining to the predictor step. For purposes of illustration, let us return to the sketch shown in Fig. B.1 and focus on the calculations associated with

Table B.1 | Nozzle shape and initial conditions

$\dfrac{x}{L}$	$\dfrac{A}{A^*}$	$\dfrac{\rho}{\rho_o}$	$\dfrac{V}{a_o}$	$\dfrac{T}{T_o}$
0	5.950	1.000	0.100	1.000
0.1	5.312	0.969	0.207	0.977
0.2	4.718	0.937	0.311	0.954
0.3	4.168	0.906	0.412	0.931
0.4	3.662	0.874	0.511	0.907
0.5	3.200	0.843	0.607	0.884
0.6	2.782	0.811	0.700	0.861
0.7	2.408	0.780	0.790	0.838
0.8	2.078	0.748	0.877	0.815
0.9	1.792	0.717	0.962	0.792
1.0	1.550	0.685	1.043	0.769
1.1	1.352	0.654	1.122	0.745
1.2	1.198	0.622	1.197	0.722
1.3	1.088	0.591	1.268	0.699
1.4	1.022	0.560	1.337	0.676
1.5	1.000	0.528	1.402	0.653
1.6	1.022	0.497	1.463	0.630
1.7	1.088	0.465	1.521	0.607
1.8	1.198	0.434	1.575	0.583
1.9	1.352	0.402	1.625	0.560
2.0	1.550	0.371	1.671	0.537
2.1	1.792	0.339	1.713	0.514
2.2	2.078	0.308	1.750	0.491
2.3	2.408	0.276	1.783	0.468
2.4	2.782	0.245	1.811	0.445
2.5	3.200	0.214	1.834	0.422
2.6	3.662	0.182	1.852	0.398
2.7	4.168	0.151	1.864	0.375
2.8	4.718	0.119	1.870	0.352
2.9	5.312	0.088	1.870	0.329
3.0	5.950	0.056	1.864	0.306

grid point i. We will choose $i = 16$, which is the grid point at the throat of the nozzle drawn in Fig. B.4. From the initial data given in Table B.1, we have

$$\rho_i = \rho_{16} = 0.528$$

$$\rho_{i+1} = \rho_{17} = 0.497$$

$$V_i = V_{16} = 1.402$$

$$V_{i+1} = V_{17} = 1.463$$

$$T_i = T_{16} = 0.653$$

$$T_{i+1} = T_{17} = 0.630$$

$$\Delta x = 0.1$$

$$A_i = A_{16} = 1.0 \qquad \ln A_{16} = 0$$

$$A_{i+1} = A_{17} = 1.022 \qquad \ln A_{17} = 0.02176$$

Substitute these values into Eq. (B.13).

$$\left(\frac{\partial \rho}{\partial t}\right)_{16}^{t=0} = -0.528 \left(\frac{1.463 - 1.402}{0.1}\right) - 0.528(1.402)\left(\frac{0.02176 - 0}{0.1}\right)$$

$$- 1.402 \left(\frac{0.497 - 0.528}{0.1}\right)$$

$$= \boxed{-0.0445}$$

Substitute these values into Eq. (B.14).

$$\left(\frac{\partial V}{\partial t}\right)_{16}^{t=0} = -1.402 \left(\frac{1.463 - 1.402}{0.1}\right)$$

$$- \frac{1}{1.4}\left[\frac{0.630 - 0.653}{0.1} + \frac{0.653}{0.528}\left(\frac{0.497 - 0.528}{0.1}\right)\right]$$

$$= \boxed{-0.418}$$

Substitute these values into Eq. (B.15).

$$\left(\frac{\partial T}{\partial t}\right)_{16}^{t=0} = -1.402 \left(\frac{0.630 - 0.653}{0.1}\right) - (1.4 - 1)(0.653)$$

$$\times \left[\frac{1.463 - 1.402}{0.1} + 1.402\left(\frac{0.02176 - 0}{0.1}\right)\right]$$

$$= \boxed{0.0843}$$

Please note: The numbers shown in the *boxes* here are the precise numbers, rounded to three significant figures, that came out of the author's Macintosh computer. If you

choose to run through these calculations with your hand calculator using all these entries, there will be slight differences because the numbers you feed into the calculator are *already* rounded to three significant figures, and hence the subsequent arithmetic operations on your calculator will lead to slight errors compared to the computer results. That is, your hand-calculator results may not always give you *precisely* the numbers you will find in the boxes, but they will certainly be close enough to check the results.

The next step is to calculate the *predicted* values (the "barred" quantities) from Eqs. (B.16) to (B.18). To do this, we first note that Δt is calculated from Eq. (B.31), which picks the minimum value of Δt_i from all those calculated from Eq. (B.29) evaluated for all internal points $i = 2, 3, \ldots, 30$. We do not have the space to show all these calculations here. As a sample calculation, let us calculate $(\Delta t)_{16}^{t=0}$ from Eq. (B.29). At present, we will assume a Courant number equal to 0.5; that is, $C = 0.5$. Also, in nondimensional terms, the speed of sound is given by

$$a = \sqrt{T} \tag{B.37}$$

where in Eq. (B.37) both a and T are the *nondimensional* values (a denotes the local speed of sound divided by a_0). Derive Eq. (B.37) for yourself. Thus, from Eq. (B.29), we have

$$(\Delta t)_{16}^{t=0} = C\left[\frac{\Delta x}{(T_{16})^{1/2} + V_{16}}\right] = 0.5\left[\frac{0.1}{(0.653)^{1/2} + 1.402}\right] = 0.0226$$

This type of calculation is made at all the interior grid points, and the minimum value is chosen. The resulting minimum value is

$$\Delta t = 0.0201$$

With this, we can calculate $\bar{\rho}$, $\bar{V}$, and $\bar{T}$. From Eq. (B.16), noting that $t = 0 + \Delta t = \Delta t$,

$$\bar{\rho}_{16}^{t=\Delta t} = \rho_{16}^{t=0} + \left(\frac{\partial \rho}{\partial t}\right)_{16}^{t=0} \Delta t = 0.528 + (-0.0445)(0.0201)$$

$$= \boxed{0.527}$$

From Eq. (B.17),

$$\bar{V}_{16}^{t=\Delta t} = V_{16}^{t=0} + \left(\frac{\partial V}{\partial t}\right)_{16}^{t=0} \Delta t = 1.402 + (-0.418)(0.0201)$$

$$= \boxed{1.39}$$

From Eq. (B.18),

$$\bar{T}_{16}^{t=\Delta t} = T_{16}^{t=0} + \left(\frac{\partial T}{\partial t}\right)_{16}^{t=0} \Delta t = 0.653 + (0.0843)(0.0201)$$

$$= \boxed{0.655}$$

At this stage, we note that these calculations are carried out over *all* the internal grid points $i = 2$ to 30. The calculations are too repetitive to include here. Simply note that when the predictor step is completed, we have $\bar{\rho}$, $\bar{V}$, and $\bar{T}$ at all the internal grid points $i = 2$ to 30. This includes, of course, $\bar{\rho}_{15}^{t=\Delta t}$, $\bar{V}_{15}^{t=\Delta t}$, and $\bar{T}_{15}^{t=\Delta t}$. Focusing again on grid point 16, we now insert these *barred* quantities at grid points 15 and 16 into Eqs. (B.19) to (B.21). This is the beginning of the corrector step. From Eq. (B.19) we have

$$\left(\overline{\frac{\partial \rho}{\partial t}}\right)_{16}^{t=\Delta t} = -0.527(0.653) - 0.527(1.39)(-0.218) - 1.39(-0.368)$$

$$= \boxed{0.328}$$

From Eq. (B.20) we have

$$\left(\overline{\frac{\partial V}{\partial t}}\right)_{16}^{t=\Delta t} = -1.39(0.653) - \frac{1}{1.4}\left(-0.257 + \frac{0.655}{0.527}\right) = \boxed{-0.400}$$

From Eq. (B.21) we have

$$\left(\overline{\frac{\partial T}{\partial t}}\right)_{16}^{t=\Delta t} = -1.39(-0.257) - (1.4 - 1)(0.655)[0.653 + 1.39(-0.218)]$$

$$= \boxed{0.267}$$

With these values, we form the *average* time derivatives using Eqs. (B.22) to (B.24). From Eq. (B.22), we have at grid point $i = 16$,

$$\left(\frac{\partial \rho}{\partial t}\right)_{av} = 0.5(-0.0445 + 0.328) = \boxed{0.142}$$

From Eq. (B.23), we have at grid point $i = 16$,

$$\left(\frac{\partial V}{\partial t}\right)_{av} = 0.5(-0.418 - 0.400) = \boxed{-0.409}$$

From Eq. (B.24), we have at grid point $i = 16$,

$$\left(\frac{\partial T}{\partial t}\right)_{av} = 0.5(0.0843 + 0.267) = \boxed{0.176}$$

We now complete the corrector step by using Eqs. (B.25) to (B.27). From Eq. (B.25), we have at $i = 16$,

$$\rho_{16}^{t=\Delta t} = 0.528 + 0.142(0.0201) = \boxed{0.531}$$

From Eq. (B.26), we have at $i = 16$,

$$V_{16}^{t=\Delta t} = 1.402 + (-0.409)(0.0201) = \boxed{1.394}$$

From Eq. (B.27), we have at $i = 16$,

$$T_{16}^{t=\Delta t} = 0.653 + 0.176(0.0201) = \boxed{0.656}$$

Defining a nondimensional pressure as the local static pressure divided by the reservoir pressure p_o, the equation of state is given by

$$p = \rho T$$

where p, ρ, and T are *nondimensional* values. Thus, at grid point $i = 16$, we have

$$p_{16}^{t=\Delta t} = \rho_{16}^{t=\Delta t} T_{16}^{t=\Delta t} = 0.531(0.656) = \boxed{0.349}$$

This now completes the corrector step for grid point $i = 16$. When the above corrector-step calculations are carried out for all grid points from $i = 2$ to 30, then we have completed the corrector step for all the *internal* grid points.

It remains to calculate the flowfield variables at the boundary points. At the subsonic inflow boundary $(i = 1)$, V_1 is calculated by linear extrapolation from grid points 2 and 3. At the end of the corrector step, from a calculation identical to that given above, the values of V_2 and V_3 at time $t = \Delta t$ are $V_2 = 0.212$ and $V_3 = 0.312$. Thus, from Eq. (B.32), we have

$$V_1 = 2V_2 - V_3 = 2(0.212) - 0.312 = \boxed{0.111}$$

At the supersonic outflow boundary $(i = 31)$ all the flowfield variables are calculated by linear extrapolation from Eqs. (B.34a) to (B.34c). At the end of the corrector step, from a calculation identical to that given above, $V_{29} = 1.884$, $V_{30} = 1.890$, $\rho_{29} = 0.125$, $\rho_{30} = 0.095$, $T_{29} = 0.354$, and $T_{30} = 0.332$. When these values are inserted into Eqs. (B.34a) to (B.34c), we have

$$V_{31} = 2V_{30} - V_{29} = 2(1.890) - 1.884 = \boxed{1.895}$$

$$\rho_{31} = 2\rho_{30} - \rho_{29} = 2(0.095) - 0.125 = \boxed{0.066}$$

$$T_{31} = 2T_{30} - T_{29} = 2(0.332) - 0.354 = \boxed{0.309}$$

With this, we have completed the calculation of all the flowfield variables at all the grid points after the first time step, i.e., at time $t = \Delta t$. A tabulation of these variables is given in Table B.2. Note that the Mach number is included in this tabulation. In terms of the nondimensional velocity and temperature, the Mach number (which is already a dimensionless parameter defined as the local velocity divided by the local speed of sound) is given by

$$M = \frac{V}{\sqrt{T}} \tag{B.38}$$

Examine Table B.2 closely. By reading across the line labeled $I = 16$, you will find the familiar numbers that we have generated for grid point $i = 16$ in this discussion. Take the time to make this comparison. The entries for all other internal grid points

Table B.2 | Flowfield variables after the first time step

I	$\frac{x}{L}$	$\frac{A}{A^*}$	$\frac{\rho}{\rho_o}$	$\frac{V}{a_o}$	$\frac{T}{T_o}$	$\frac{p}{p_o}$	M
1	0.000	5.950	1.000	0.111	1.000	1.000	0.111
2	0.100	5.312	0.955	0.212	0.972	0.928	0.215
3	0.200	4.718	0.927	0.312	0.950	0.881	0.320
4	0.300	4.168	0.900	0.411	0.929	0.836	0.427
5	0.400	3.662	0.872	0.508	0.908	0.791	0.534
6	0.500	3.200	0.844	0.603	0.886	0.748	0.640
7	0.600	2.782	0.817	0.695	0.865	0.706	0.747
8	0.700	2.408	0.789	0.784	0.843	0.665	0.854
9	0.800	2.078	0.760	0.870	0.822	0.625	0.960
10	0.900	1.792	0.731	0.954	0.800	0.585	1.067
11	1.000	1.550	0.701	1.035	0.778	0.545	1.174
12	1.100	1.352	0.670	1.113	0.755	0.506	1.281
13	1.200	1.198	0.637	1.188	0.731	0.466	1.389
14	1.300	1.088	0.603	1.260	0.707	0.426	1.498
15	1.400	1.022	0.567	1.328	0.682	0.387	1.609
16	1.500	1.000	0.531	1.394	0.656	0.349	1.720
17	1.600	1.022	0.494	1.455	0.631	0.312	1.833
18	1.700	1.088	0.459	1.514	0.605	0.278	1.945
19	1.800	1.198	0.425	1.568	0.581	0.247	2.058
20	1.900	1.352	0.392	1.619	0.556	0.218	2.171
21	2.000	1.550	0.361	1.666	0.533	0.192	2.282
22	2.100	1.792	0.330	1.709	0.510	0.168	2.393
23	2.200	2.078	0.301	1.748	0.487	0.146	2.504
24	2.300	2.408	0.271	1.782	0.465	0.126	2.614
25	2.400	2.782	0.242	1.813	0.443	0.107	2.724
26	2.500	3.200	0.213	1.838	0.421	0.090	2.834
27	2.600	3.662	0.184	1.858	0.398	0.073	2.944
28	2.700	4.168	0.154	1.874	0.376	0.058	3.055
29	2.800	4.718	0.125	1.884	0.354	0.044	3.167
30	2.900	5.312	0.095	1.890	0.332	0.032	3.281
31	3.000	5.950	0.066	1.895	0.309	0.020	3.406

are calculated in a like manner. Also note the values at the boundary points, labeled $I = 1$ and $I = 31$ in Table B.2. You will find the numbers to be the same as discussed here.

FINAL NUMERICAL RESULTS: THE STEADY-STATE SOLUTION

Compare the flowfield results obtained after one time step (Table B.2) with the same quantities at the previous time (in this case the initial conditions given in Table B.1). Comparing these two tables, we see that the flowfield variables *have changed*. For example, the nondimensional density at the throat (where $A = 1$) has changed from 0.528 to 0.531, a 0.57 percent change over one time step. This is the natural behavior of a time-marching solution—the flowfield variables change from one time step

to the next. However, in the approach toward the steady-state solution, at larger values of time (after a large number of time steps), the *changes* in the flowfield variables from one time step to the next become smaller and approach zero in the limit of large time. At this stage, the steady state (for all practical purposes) has been achieved, and the calculation can be stopped. This termination of the calculation can be done automatically by the computer program itself by having a test in the program to sense when the changes in the flowfield variables become smaller than some prescribed value (prescribed by you, depending on your desired accuracy of the final "steady-state" solution). Another option, and that preferred by the present author, is to simply stop the calculation after a prescribed number of time steps, look at the results, and see if they have approached the stage where the flowfield variables are not materially changing any more. If such is not the case, simply resume the calculations, and carry them out for the requisite number of time steps until you do see that the steady-state results have been reached.

What patterns do the timewise variations of the flowfield variables take? Some feeling for the answer is provided by Fig. B.5, which shows the variation of ρ, T, p, and M at the nozzle throat plotted versus the number of time steps. The abscissa starts at zero, which represents the initial conditions, and ends at time step 1000. Hence, the abscissa is essentially a time axis, with time increasing to the right. Note that the largest changes take place at early times, after which the final, steady-state value is approached almost asymptotically. Here is the "rubber band effect" mentioned previously; at early times the rubber band is "stretched" tightly, and therefore the flowfield variables are driven by a stronger potential and hence change rapidly. At later times, as the steady state is approached, the rubber band is less stretched; it becomes more "relaxed," and the changes become much smaller with time. The dashed lines to the right of the curves shown in Fig. B.5 represent the exact, analytical values as obtained from the equations discussed in Chap. 5. Note that the numerical time-marching procedure converges to the proper theoretical steady-state answer. We also note that no artificial viscosity has been explicitly added for these calculations; it is not needed.

It is interesting to examine the variation of the time derivatives as a function of time itself, or equivalently as a function of the number of time steps. Once again focusing on the nozzle throat (at grid point $i = 16$), Fig. B.6 gives the variation of the time derivatives of nondimensional density and velocity as a function of the number of time steps. These are the *average* time derivatives calculated from Eqs. (B.22) and (B.23), respectively. The *absolute value* of these time derivatives is shown in Fig. B.6. From these results, note two important aspects:

1. At early times, the time derivatives are large, and they oscillate in value. These oscillations are associated with various unsteady compression and expansion waves that propagate through the nozzle during the transient process. (See Chap. 7.)

2. At later times, the time derivatives rapidly grow small, changing by six orders of magnitude over a span of 1000 time steps. This is, of course, what we want to see happen. In the theoretical limit of the steady state (which is achieved at infinite time), the time derivatives should go to zero. However, numerically
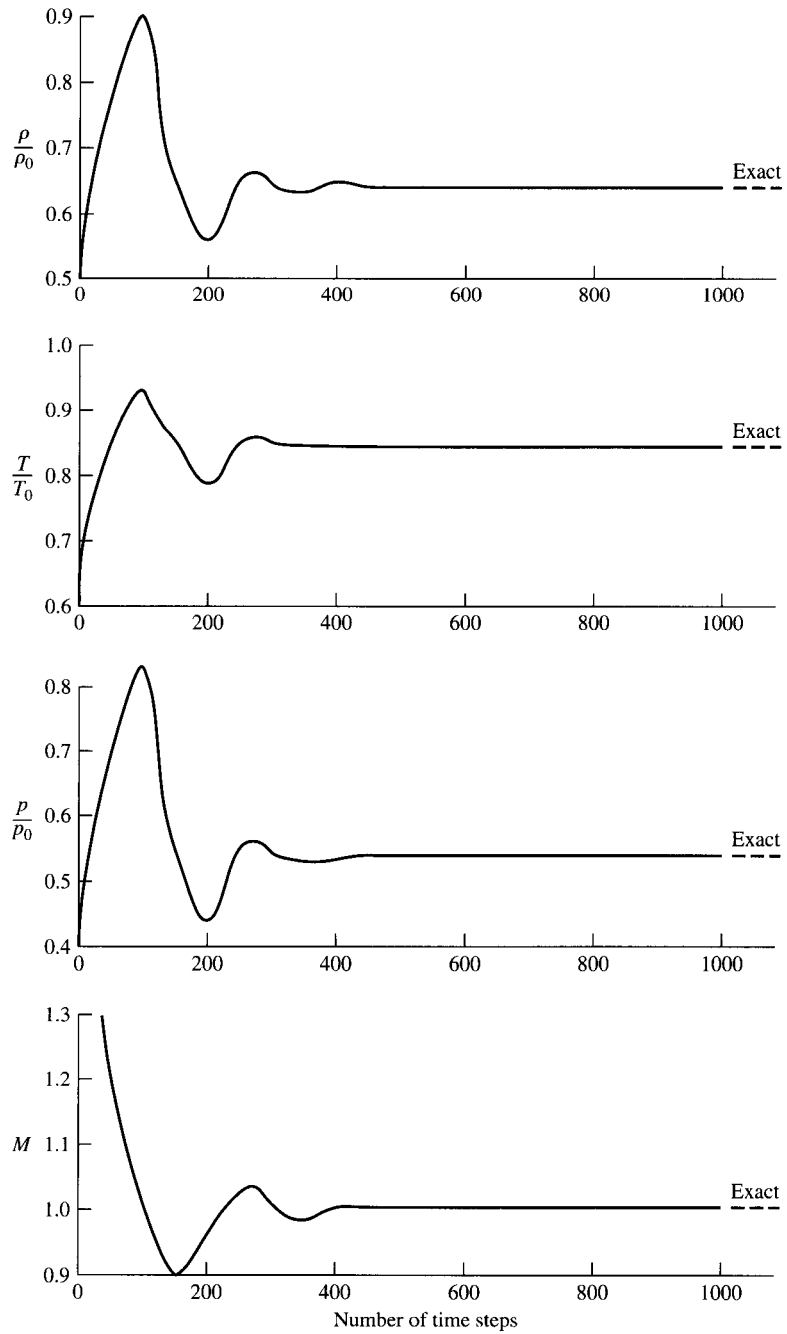
Figure B.5 | Timewise variations of the density, temperature, pressure, and Mach number at the nozzle throat (at grid point $i = 15$, where $A = 1$).
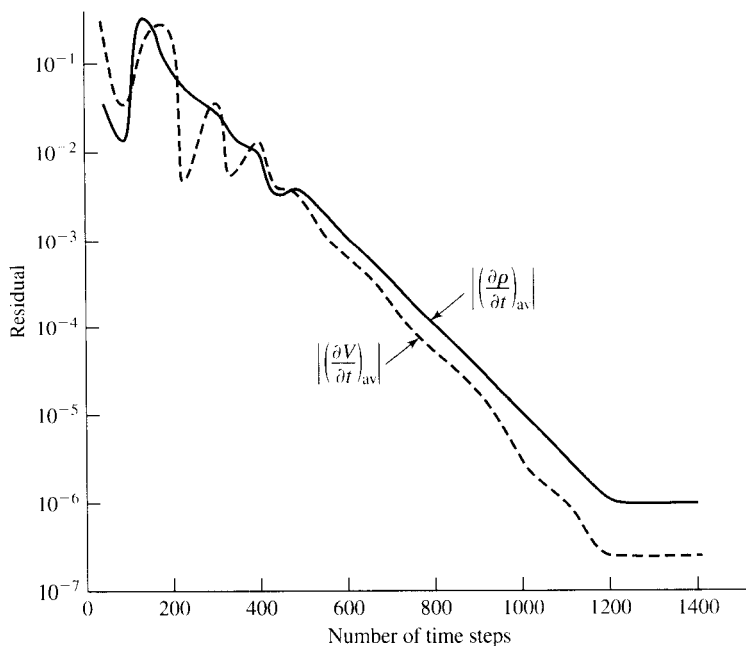
Figure B.6 | Timewise variations of the absolute values of the time derivatives of nondimensional density and velocity at the nozzle throat (at grid point $i = 16$).

this will never happen over a finite number of time steps. In fact, the results shown in Fig. B.6 indicate that the values of the time derivatives plateau after 1200 time steps. This seems to be a characteristic of MacCormack's technique. However, the values of the time derivatives at these plateaus are so small that, for all practical purposes, the numerical solution has arrived at the steady-state solution. Indeed, in terms of the values of the flowfield variables themselves, the results of Fig. B.5 indicate that the steady state is realistically achieved after 500 time steps, during which the time derivatives in Fig. B.6 have decreased only by two orders of magnitude.

Return to Eqs. (B.8) and (B.10) for a moment; we might visualize that what is being plotted in Fig. B.6 are the numerical values of the right-hand side of these equations. As time progresses and as the steady state is approached, the right-hand side of these equations should approach zero. Since the *numerical* values of the right-hand side are not precisely zero, they are called *residuals*. This is why the ordinate in Fig. B.6 is labeled as the residual. When CFD experts are comparing the relative merits of two or more different algorithms for a time-marching solution to the steady state, the magnitude of the residuals and their rate of decay are often used as figures of merit. That algorithm that gives the fastest decay of the residuals to the smallest value is usually looked upon most favorably.
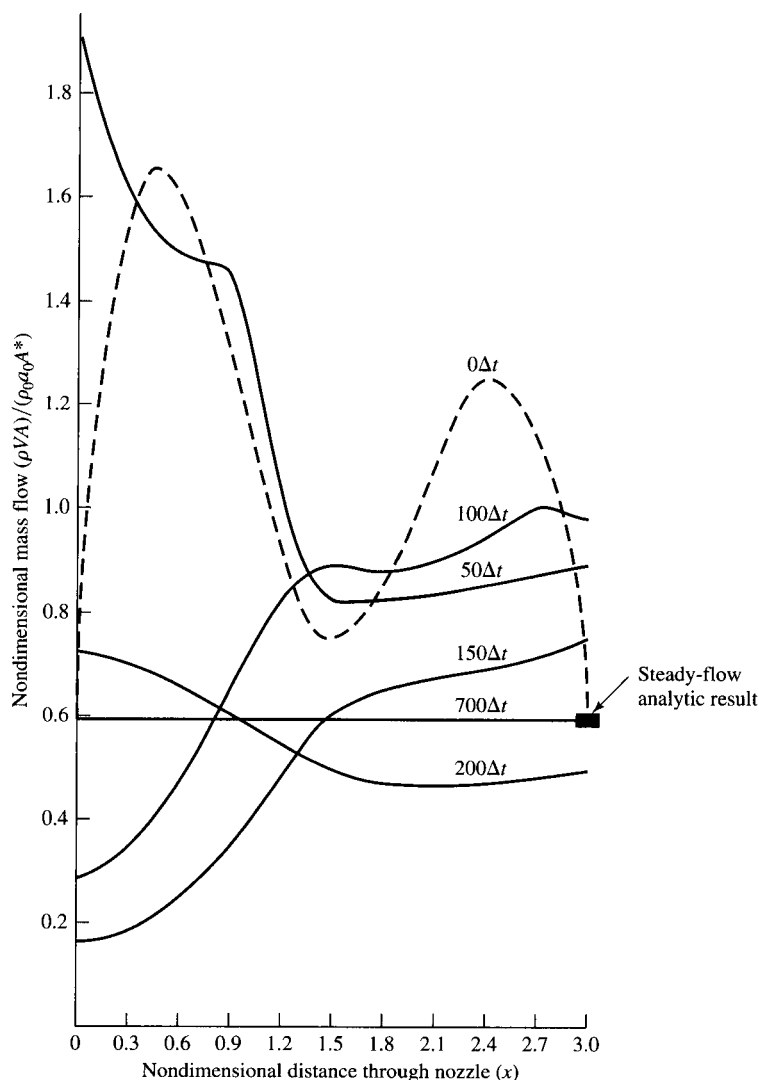
Figure B.7 | Instantaneous distributions of the nondimensional mass flow as a function of distance through the nozzle at six different times during the time-marching approach to the steady state.

Another insight to the mechanics of the timewise variation of the flow and its approach to the steady state is provided by the mass flow variations shown in Fig. B.7. Here, the nondimensional mass flow ρVA (where ρ, V, and A are the nondimensional values) is plotted as a function of nondimensional distance through the nozzle. Six different curves are shown, each for a different time during the course of the time-marching procedure. The dashed curve is the variation of ρVA, which

pertains to the initial conditions, and hence it is labeled $0\Delta t$. The strange-looking, distorted sinelike variation of this dashed curve is simply the product of the assumed initial values for ρ and V combined with the specified parabolic variation of the nozzle area ratio A. After 50 time steps, the mass flow distribution through the nozzle has changed considerably; this is given by the curve labeled $50\Delta t$. After 100 time steps ($100\Delta t$), the mass flow distribution has changed radically; the mass flow variation is simply flopping around inside the nozzle due to the transient variation of the flowfield variables. However, after 200 time steps ($200\Delta t$), the mass flow distribution is beginning to settle down, and after 700 time steps ($700\Delta t$), the mass flow distribution is a straight, horizontal line across the graph. This says that the mass flow has converged to a *constant*, steady-state value throughout the nozzle. This agrees with our basic knowledge of steady-state nozzle flows, namely, that

$$\rho VA = \text{constant}$$

Moreover, it has converged to essentially the *correct value* of the steady mass flow, which in terms of the *nondimensional* variables evaluated at the nozzle throat is given by

$$\rho VA = \rho^* \sqrt{T^*} \qquad \text{(at throat)} \qquad (B.39)$$

where ρ^* and T^* are the nondimensional density and temperature at the throat, and where $M = 1$. [Derive Eq. (B.39) yourself—it is easy.] From the analytical equations discussed in Chap. 5, when $M = 1$ and $\gamma = 1.4$, we have $\rho^* = 0.634$ and $T^* = 0.833$. With these numbers, Eq. (B.39) yields

$$\rho VA = \text{constant} = 0.579$$

This value is given by the dark square in Fig. B.7; the mass flow result for $700\Delta t$ agrees reasonably well with the dark square.

Finally, let us examine the steady-state results. From our discussion and from examining Fig. B.5, the steady state is, for all practical purposes, reached after about 500 time steps. However, being very conservative, we will examine the results obtained after 1400 time steps; between 700 and 1400 time steps, there is no change in the results, at least to the three-decimal-place accuracy given in the tables herein.

A feeling for the graphical accuracy of the numerically obtained steady state is given by Fig. B.8. Here, the steady-state nondimensional density and Mach number distributions through the nozzle are plotted as a function of nondimensional distance along the nozzle. The numerical results, obtained after 1400 time steps, are given by the solid curves, and the exact analytical results are given by the circles. The analytical results are obtained from the equations discussed in Chap. 5; they can readily be obtained from the tables in App. A. They can also be obtained by writing your own short computer program to calculate numbers from the theoretically derived equations in Chap. 5. In any event, the comparison shown in Fig. B.8 clearly demonstrates that the numerical results agree very well with the exact analytical values, certainly to within graphical accuracy.

The detailed numerical results, to three decimal places, are tabulated in Table B.3. These are the results obtained after 1400 time steps. They are given here for you to
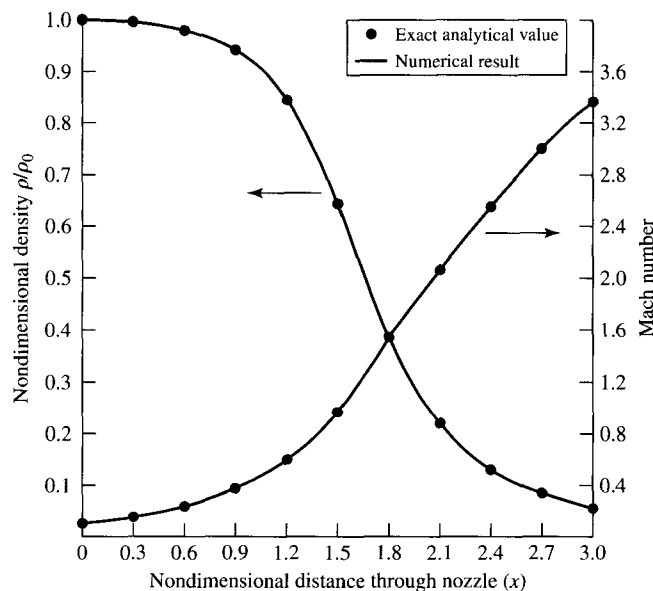
Figure B.8 | Steady-state distributions of nondimensional density and Mach number as a function of nondimensional distance through the nozzle. Comparison between the exact analytical values (circles) and the numerical results (solid curves).

compare numbers from your own computer program. It is interesting to note that the elapsed nondimensional time, starting at zero with the initial conditions, is, after 1400 time steps, a value of 28.952. Since time is nondimensionalized by the quantity L/a_o, let us assume a case where the length of the nozzle is 1 m and the reservoir temperature is the standard sea level value, $T = 288$ K. For this case, $L/a_o = (1\text{ m})/(340.2\text{ m/s}) = 2.94 \times 10^{-3}$ s. Hence, the total *real* time that has elapsed over the 1400 time steps is $(2.94 \times 10^{-3})(28.952) = 0.0851$ s. That is, the nozzle flow, starting from the assumed initial conditions, takes only 85.1 ms to reach steady-state conditions; in reality, since convergence is obtained for all practical purposes after about 500 time steps, the practical convergence time is more on the order of 30 ms.

A comparison between some of the numerical results and the corresponding exact analytical values is given in Table B.4; this provides you with a more detailed comparison than is given in Fig. B.8. Compared are the numerical and analytical results for the density ratio and Mach number. Note that the numerical results, to three decimal places, are not in precise agreement with the analytical values; there is a small percentage disagreement between the two sets of results, ranging from 0.3 to 3.29 percent. This amount of error is not discernable on the graphical display in Fig. B.8. At first thought, there might be three reasons for these small numerical inaccuracies: (1) a small inflow boundary condition error, (2) truncation errors associated with the

Table B.3 | Flowfield variables after 1400 time steps (nonconservation form of the governing equations)

I	$\dfrac{x}{L}$	$\dfrac{A}{A^*}$	$\dfrac{\rho}{\rho_o}$	$\dfrac{V}{a_o}$	$\dfrac{T}{T_o}$	$\dfrac{p}{p_o}$	M	$\dot{m}$
1	0.000	5.950	1.000	0.099	1.000	1.000	0.099	0.590
2	0.100	5.312	0.998	0.112	0.999	0.997	0.112	0.594
3	0.200	4.718	0.997	0.125	0.999	0.996	0.125	0.589
4	0.300	4.168	0.994	0.143	0.998	0.992	0.143	0.591
5	0.400	3.662	0.992	0.162	0.997	0.988	0.163	0.589
6	0.500	3.200	0.987	0.187	0.995	0.982	0.187	0.589
7	0.600	2.782	0.982	0.215	0.993	0.974	0.216	0.588
8	0.700	2.408	0.974	0.251	0.989	0.963	0.252	0.588
9	0.800	2.078	0.963	0.294	0.985	0.948	0.296	0.587
10	0.900	1.792	0.947	0.346	0.978	0.926	0.350	0.587
11	1.000	1.550	0.924	0.409	0.969	0.895	0.416	0.586
12	1.100	1.352	0.892	0.485	0.956	0.853	0.496	0.585
13	1.200	1.198	0.849	0.575	0.937	0.795	0.594	0.585
14	1.300	1.088	0.792	0.678	0.911	0.722	0.710	0.584
15	1.400	1.022	0.721	0.793	0.878	0.633	0.846	0.584
16	1.500	1.000	0.639	0.914	0.836	0.534	0.099	0.584
17	1.600	1.022	0.551	1.037	0.789	0.434	1.167	0.584
18	1.700	1.088	0.465	1.155	0.737	0.343	1.345	0.584
19	1.800	1.198	0.386	1.263	0.684	0.264	1.528	0.585
20	1.900	1.352	0.318	1.361	0.633	0.201	1.710	0.586
21	2.000	1.550	0.262	1.446	0.585	0.153	1.890	0.587
22	2.100	1.792	0.216	1.519	0.541	0.117	2.065	0.588
23	2.200	2.078	0.179	1.582	0.502	0.090	2.233	0.589
24	2.300	2.408	0.150	1.636	0.467	0.070	2.394	0.590
25	2.400	2.782	0.126	1.683	0.436	0.055	2.549	0.590
26	2.500	3.200	0.107	1.723	0.408	0.044	2.696	0.591
27	2.600	3.662	0.092	1.759	0.384	0.035	2.839	0.591
28	2.700	4.168	0.079	1.789	0.362	0.029	2.972	0.592
29	2.800	4.718	0.069	1.817	0.342	0.024	3.105	0.592
30	2.900	5.312	0.061	1.839	0.325	0.020	3.225	0.595
31	3.000	5.950	0.053	1.862	0.308	0.016	3.353	0.585

finite value of Δx, and (3) possible effects of the Courant number being substantially less than unity (recall that in the calculations discussed so far, the Courant number is chosen to be 0.5). Let us examine each of these reasons in turn.

Inflow Boundary Condition Error

There is a "built-in" error at the inflow boundary. At the first grid point, at $x = 0$, we *assume* that the density, pressure, and temperature are the reservoir properties ρ_o, p_o, and T_o, respectively. This is strictly true only if $M = 0$ at this point. In reality, there is a finite area ratio at $x = 0$, namely, $A/A^* = 5.95$, and hence a finite Mach number must exist at $x = 0$, both numerically and analytically (to allow a finite value of mass flow through the nozzle). Hence, in Table B.4, the numerical value of ρ/ρ_o at $x = 0$ is equal to 1.0—this is our prescribed boundary condition. On the other hand, the exact

Table B.4 | Density ratio and Mach number distributions through the nozzle

$\frac{x}{L}$	$\frac{A}{A^*}$	$\frac{\rho}{\rho_o}$ (numerical results)	$\frac{\rho}{\rho_o}$ (exact analytical results)	Difference, %	M (numerical results)	M (exact analytical results)	Difference, %
0.000	5.950	1.000	0.995	0.50	0.099	0.098	1.01
0.100	5.312	0.998	0.994	0.40	0.112	0.110	1.79
0.200	4.718	0.997	0.992	0.30	0.125	0.124	0.08
0.300	4.168	0.994	0.990	0.40	0.143	0.140	2.10
0.400	3.662	0.992	0.987	0.50	0.163	0.160	1.84
0.500	3.200	0.987	0.983	0.40	0.187	0.185	1.07
0.600	2.782	0.982	0.978	0.41	0.216	0.214	0.93
0.700	2.408	0.974	0.970	0.41	0.252	0.249	1.19
0.800	2.078	0.963	0.958	0.52	0.296	0.293	1.01
0.900	1.792	0.947	0.942	0.53	0.350	0.347	0.86
1.000	1.550	0.924	0.920	0.43	0.416	0.413	0.72
1.100	1.352	0.892	0.888	0.45	0.496	0.494	0.40
1.200	1.198	0.849	0.844	0.59	0.594	0.592	0.34
1.300	1.088	0.792	0.787	0.63	0.710	0.709	0.14
1.400	1.022	0.721	0.716	0.69	0.846	0.845	0.12
1.500	1.000	0.639	0.634	0.78	0.999	1.000	0.10
1.600	1.022	0.551	0.547	0.73	1.167	1.169	0.17
1.700	1.088	0.465	0.461	0.87	1.345	1.348	0.22
1.800	1.198	0.386	0.382	1.04	1.528	1.531	0.20
1.900	1.352	0.318	0.315	0.94	1.710	1.715	0.29
2.000	1.550	0.262	0.258	1.53	1.890	1.896	0.32
2.100	1.792	0.216	0.213	1.39	2.065	2.071	0.29
2.200	2.078	0.179	0.176	1.68	2.233	2.240	0.31
2.300	2.408	0.150	0.147	2.00	2.394	2.402	0.33
2.400	2.782	0.126	0.124	2.38	2.549	2.557	0.31
2.500	3.200	0.107	0.105	1.87	2.696	2.706	0.37
2.600	3.662	0.092	0.090	2.17	2.839	2.848	0.32
2.700	4.168	0.079	0.078	1.28	2.972	2.983	0.37
2.800	4.718	0.069	0.068	1.45	3.105	3.114	0.29
2.900	5.312	0.061	0.059	3.29	3.225	3.239	0.43
3.000	5.950	0.053	0.052	1.89	3.353	3.359	0.18

analytical value of ρ/ρ_o at $x = 0$ is 0.995, giving a 0.5 percent error. This built-in error is not viewed as serious, and we will not be concerned with it here.

Truncation Error: The Matter of Grid Independence

The matter of *grid independence* is a serious consideration in CFD, and this stage of our data analysis is a perfect time to introduce the concept. In general, when you solve a problem using CFD, you are employing a finite number of grid points (or a finite mesh) distributed over the flow field. Assume that you are using N grid points. If everything goes well during your solution, you will get some numbers out for the flowfield variables at these N grid points, and these numbers may look qualitatively

good to you. However, assume that you rerun your solution, this time using twice as many grid points, $2N$, distributed over the same domain; i.e., you have decreased the value of the increment Δx (and also Δy in general, if you are dealing with a two-dimensional solution). You may find that the values of your flowfield variables are quite different for this second calculation. If this is the case, then your solution is a function of the number of grid points you are using—an untenable situation. You must, if at all practical, continue to increase the number of grid points until you reach a solution which is no longer sensitive to the number of points. When you reach this situation, then you have achieved *grid independence*.

Question: Do we have grid independence for the present calculation? Recall that we have used 31 grid points distributed evenly through the nozzle. To address this question, let us double the number of grid points; i.e., let us halve the value of Δx by using 61 grid points. Table B.5 compares the steady-state results for density, temperature, and pressure ratios, as well as for Mach numbers, at the throat for both the cases using 31 and 61 grid points. Also tabulated in Table B.5 are the exact analytical results. Note that although doubling the number of grid points did improve the numerical solution, it did so only marginally. The same is true for all locations within the nozzle. In other words, the two steady-state numerical solutions are essentially the same, and therefore we can conclude that our original calculations using 31 grid points is essentially *grid-independent*. This grid-independent solution does not agree *exactly* with the analytical results, but it is certainly close enough for our purposes. The degree of grid independence that you need to achieve in a given problem depends on what you want out of the solution. Do you need extreme accuracy? If so, you need to press the matter of grid independence in a very detailed fashion. Can you tolerate answers that can be a little less precise numerically (such as the 1 or 2 percent accuracy shown in the present calculations)? If so, you can slightly relax the criterion for extreme grid independence and use fewer grid points, thus saving computer time (which frequently means saving money). The proper decision depends on the circumstances. However, you should always be conscious of the question of grid independence and resolve the matter to your satisfaction for any CFD problem you solve. For example, in the present problem, do you think you can drive the numerical results shown in Table B.5 to agree exactly with the analytical results by using more and more grid points? If so, how many grid points will you need? You might want to experiment with this question by running your own program and seeing what happens.

Table B.5 | Demonstration of grid independence

	Conditions at the nozzle throat			
	$\dfrac{\rho^*}{\rho_o}$	$\dfrac{T^*}{T_o}$	$\dfrac{p^*}{p_o}$	M
Case 1: 31 points	0.639	0.836	0.534	0.999
Case 2: 61 points	0.638	0.835	0.533	1.000
Exact analytical solution	0.634	0.833	0.528	1.000

Courant Number Effects

There is the possibility that if the Courant number is too small, there might be problems in regard to the accuracy of the solution, albeit the solution will be very stable. Do we have such a problem with the present calculations? We have employed $C = 0.5$ for the present calculations. Is this too small, considering that the stability criterion for *linear* hyperbolic equations is $C \leq 1.0$? To examine this question, we can simply repeat the previous calculations but with progressively higher values of the Courant number. The resulting steady-state flowfield values at the nozzle throat are tabulated in Table B.6; the tabulations are given for six different values of C, starting at $C = 0.5$ and ranging to 1.2. For values ranging to as high as $C = 1.1$, the results were only marginally different, as seen in Table B.6. By increasing C to as high as 1.1, the numerical results do not agree any better with the exact analytical results (as shown in Table B.6) than the results at lower values of C. Hence, all our previous results obtained by using $C = 0.5$ are not tainted by any noticeable error due to the smaller-than-necessary value of C. Indeed, if anything, the numerical results for $C = 0.5$ in Table B.6 are marginally *closer* to the exact analytical solution than the results for higher Courant numbers. For the steady-state numerical results tabulated in Table B.6, the number of time steps was adjusted each time C was changed so that the nondimensional time at the end of each run was essentially the same. This adjustment is necessary because the value of Δt calculated from Eqs. (B.28) and (B.31) will obviously be different for different values of C. For example, when $C = 0.5$ as in our previous results, we carried out the time-marching procedure to 1400 time steps, which corresponded to a nondimensional time of 28.952. When C is increased to 0.7, the number of time steps carried out was $1400(\frac{5}{7}) = 1000$. This corresponded to a nondimensional time of 28.961—essentially the same as for the previous run. In the same manner, all the numerical data compared in Table B.6 pertain to the same nondimensional time.

It is interesting to note that for the present application, the CFL criterion, namely, that $C \leq 1$, does not hold exactly. In Table B.6, we show results where $C = 1.1$; a stable solution is obtained in spite of the fact that the CFL criterion is violated. However, as noted in Table B.6, when the Courant number is increased to 1.2, instabilities do occur, and the program blows up. Therefore, for the flow problem we

Table B.6 | Courant number effects

Courant number	$\dfrac{\rho^*}{\rho_o}$	$\dfrac{T^*}{T_o}$	$\dfrac{p^*}{p_o}$	M
0.5	0.639	0.836	0.534	0.999
0.7	0.639	0.837	0.535	0.999
0.9	0.639	0.837	0.535	0.999
1.0	0.640	0.837	0.535	0.999
1.1	0.640	0.837	0.535	0.999
1.2	Program went unstable and blew up			
Exact analytical solution	0.634	0.833	0.528	1.000